Modeling Brain Anatomy with 3D Arrangements of Curves

W. Mio* J. C. Bowers† M. K. Hurdal* X. Liu†

*Department of Mathematics and †Department of Computer Science
Florida State University, Tallahassee, FL 32306 USA

mio@math.fsu.edu, bowers@cs.fsu.edu, mhurdal@math.fsu.edu, xliu@cs.fsu.edu

Abstract

We employ 3D arrangements of curves to represent and analyze biological shapes, in particular, the anatomy of the human brain. The arrangements of curves may vary from fairly sparse – such as a collection of sulcal lines that coarsely approximates the global shape of the brain – to very dense decompositions of the cortical surface into space curves. A space of shapes of such arrangements is constructed equipped with geodesic metrics that can be used in conjunction with curve registration techniques to quantify shape resemblance or dissimilarity, as well as to identify the regions where anatomical differences are most pronounced. The metric is applied to the parcellation and labeling of configurations associated with the left and right hemispheres of the brain. Examples are also given of geodesic interpolations between decompositions into space curves of surfaces representing the entire left hemisphere of the brain.

1. Introduction

It is well known that the human brain varies considerably in the size, shape and extent of its folding patterns [4]. It is estimated that 60-70% of the cortex is buried in the folds. Additionally, the shape of the cortex changes as we age [22], as well as with conditions such as Alzheimer's disease, schizophrenia or bipolar disorder [1, 23, 13].

Some changes in function occur on a widespread scale, affecting many regions of the cortex, while other aspects of functional activity may be more localized. For example, some morphological differences have been demonstrated in speech and language areas. Increased white matter volumes have been found in regions of the perisylvian speech and language areas and in prefrontal and sensorimotor areas of the right hemisphere (including the superior temporal gyrus, precentral gyrus and inferior frontal gyrus) for stutterers as compared to non-stutterers [8]. These differences may be related to the known left-hemisphere dominance for speech. Interhemispheric differences in the primary auditory cortex have also been detected [14, 20]. It would seem plausible then, that hemispheric morphological differences on the cortex could be detected by shape characteristics.

Increasingly, geometric properties of the cortex are being used to study and quantify these changes. To date, most studies have focused on cortical thickness or volume [2, 16, 6]. However, these features may not demonstrate more subtle changes in the cortex and may only become apparent with large changes, or after a disease has progressed significantly. It is important to be able to identify changes in the cortex as early as possible. However, to be able to identify changes that are related to diseases, one also needs to understand what constitutes normal variations in the cortex, including those due to aging and gender.

Computational anatomy and image processing methods enable us to reconstruct the cortical surface S as a triangulated mesh from magnetic resonance imaging (MRI) scans. Typically, the cortical surface of the gray matter (GM) or white matter (WM) is reconstructed. The GM cortical surface is the interface between the GM and the cerebrospinal fluid and the WM surface is the interface between the GM and WM. In this paper, we develop techniques to represent and analyze both the entire cortical surface and subsets of features consisting of sulcal paths or sulcal curves, which give a coarse approximation to the global anatomy of the brain. We shall employ arrangements of curves in 3D space to represent a shape. These arrangements of curves may consist of a fairly sparse sets of curves that only encode large-scale anatomical properties, but they may also represent a very dense decomposition of a surface into space curves. We develop a novel framework to analyze the shape of such configurations. We construct shape spaces of arrangements of parametric curves equipped with geodesic metrics derived from Sobolev metrics that can be utilized to quantify anatomical similarity or divergence. The metric is used in conjunction with shape registration techniques that are employed to extract "preferred" parametrizations for shape comparison. Both the registration techniques and the metric are dependent upon the entire configuration, so

that they do not simply capture dissimilarities observed in individual curves in the arrangement. As the metric is obtained via integration of local contributions, the method also allow us to detect areas where morphological differences are most pronounced.

We employ the shape metric in the classification and labeling of arrangements of sulcal curves representing the left and right hemispheres of the brain. We also offer examples of geodesic interpolations of arrangements associated with the entire left hemispheres of different brains. The ability to estimate such deformations is an important step towards developing statistical models of normal shape variations in the cortex, as well as those associated with diseases.

A word about the organization of the paper: in Section 2, we construct geodesic shape spaces of arrangements of 3D space curves, including algorithmic procedures to calculate geodesic distances and geodesic paths associated with first-order Sobolev metrics; we also introduce energy density functions that encode the local contributions to the global shape distance; in Section 3, we extend curve registration techniques implemented via dynamic programming to obtain balanced parametrizations that optimally match the geometric features of the arrangements for shape comparison and apply the methodology to the classification and labeling of arrangements of sulcal curves associated with the right and left hemispheres of the brain; in Section 4, we investigate techniques to parameterize and register spherical surfaces to obtain compatible decompositions of surfaces into space curves for shape comparison – the techniques are applied to representations of hemispheres of the brain to estimate geodesic shape deformations; the last section presents a summary of the paper and a discussion of context and future work.

2. Arrangements of 3D Curves

We model brain anatomy and the shape of other 3D objects employing a collection of n parametric curves in 3-dimensional Euclidean space $\mathbb{R}^3$. Such configurations of curves may range from fairly sparse to very dense representations of 3D shapes. Each curve in the family may be an open arc or a closed curve. To simplify the presentation, in this section, we assume that all components are open arcs; however, any combination of these can be treated in an identical manner.

Let $I = [0, 1]$ and $\alpha_j \colon I \to \mathbb{R}^3$, $1 \leqslant j \leqslant n$, a collection of n parametric curves. Write the x, y and z coordinates of the curve α_j as α_{ij}, $i = 1, 2, 3$, respectively. Then, the arrangement of curves can be represented by the $3 \times n$ matrix $A = (\alpha_{ij})$. Note that each entry of A is a function $\alpha_{ij} \colon I \to \mathbb{R}$. The jth column of A simply records the coordinate functions of the curve α_j.

Given functions $f, g \colon I \to \mathbb{R}$, consider the Sobolev inner product

$$\langle f, g \rangle_1 = a \int_0^1 f(s)g(s)\, ds + b \int_0^1 f'(s)g'(s)\, ds, \quad (1)$$

where $a, b > 0$ are arbitrary weights. This induces an inner product on the vector space of arrangements of curves, as follows:

$$\langle A, B \rangle = \sum_{i=1}^{3} \sum_{j=1}^{n} \langle \alpha_{ij}, \beta_{ij} \rangle_1 , \quad (2)$$

which is simply the sum of the inner products of the corresponding entries. As usual, the norm of A is defined as $\|A\| = \sqrt{\langle A, A \rangle}$.

In order to compare the shapes of such arrangements, in analogy with Kendall's theory of shapes [9], we first introduce normalizations that will make the representation independent of translations and scale. Translational invariance can be obtained by requiring that the centroid of an arrangement A be located at the origin; that is, for each i, $1 \leqslant i \leqslant 3$,

$$\sum_{j=1}^{n} \int_0^1 \alpha_{ij}(s)\, ds = 0. \quad (3)$$

These three conditions simply constrain A to a linear subspace H of the space of matrices.

Scale invariance is also easily achieved by requiring that A have unit norm. This further constrains A to the unit sphere of H with respect to the norm $\|A\|$. For $A \neq 0$, the mapping $A \mapsto A/\|A\|$ standardizes scale and places the matrix A on the unit sphere. Heretofore, we assume that all arrangements are centered at 0 and scaled to have norm 1. We refer to such normalized arrangements as *pre-shapes*.

As in Kendall's shape theory, the invariance of shape representation under rotations – or, more generally, orthogonal transformations – is more subtle and is not achieved via a normalization of A. This reflects the fact that optimal alignment under rotations and reflections depends on the specific pair of shapes being compared.

2.1. Orthogonal Alignment

Let A, B be pre-shapes associated with 3D arrangements of n curves. A 3×3 orthogonal matrix U acts on B by applying the transformation to each of the curves in the arrangement; that is,

$$UB = \begin{bmatrix} U\beta_1 & \dots & U\beta_n \end{bmatrix}. \quad (4)$$

For example, if U is a rotation matrix, UB is the matrix that represents the rotated arrangement. For any $U \in O(3)$, the pre-shapes B and UB have the same shape. Thus, the shape s_B is defined as the orbit of B under the action of the orthogonal group $O(3)$. The geodesic shape distance $d(s_A, s_B)$ is defined as the minimum of the geodesic

distances between pre-shapes on the orbits of A and B, where the geodesic distance between pre-shapes is simply the length of the shortest arc of great circle between them on the unit sphere of H.

To calculate $d(s_A, s_B)$ and the geodesic shape deformation, it suffices to fix A and find the point on the orbit of B closest to A; that is,

$$d(s_A, s_B) = \min_{U \in O(k)} d(A, UB)\,; \tag{5}$$

this is due to the fact that the action of U is rigid; that is, preserves distance between configurations. Hence, the task is reduced to finding $U \in O(3)$ that places UB closest to A in the pre-shape sphere. Note that minimizing $d(A, UB)$ is equivalent to finding $\hat{U} \in O(3)$ that minimizes the chord distance $\|A - UB\|$. This formulation allows us to extend the classical arguments to the Sobolev metric setting and derive the following calculation of $\hat{U}$. Define AB^T to be the 3×3 matrix whose (i, j)-entry is the scalar

$$m_{ij} = \sum_{\ell=1}^{n} \langle \alpha_{i\ell}, \beta_{j\ell} \rangle_1\,. \tag{6}$$

Let $AB^T = V_1 \Sigma V_2^T$ be a singular value decomposition of AB^T, with $V_1, V_2 \in O(3)$ and Σ diagonal with non-negative eigenvalues. Then, $\hat{U} = V_1 V_2^T$ and the shape distance is given by

$$d(s_A, s_B) = \omega\,, \tag{7}$$

where $\omega = \arccos(\operatorname{tr}\Sigma)$. Letting $\hat{B} = \hat{U}B$, the geodesic distance is realized by the following arc of great circle in the pre-shape sphere:

$$\Lambda(t) = \cos(\omega t)\, A + \sin(\omega t) v(A, B)\,, \tag{8}$$

where

$$v(A, B) = \frac{\hat{B} - (\operatorname{tr}\Sigma)\, A}{\|\hat{B} - (\operatorname{tr}\Sigma)\, A\|}\,, \tag{9}$$

$0 \leqslant t \leqslant 1$, provided that $\hat{B} \neq A$. If $\hat{B} = A$, the shapes are the same and the geodesic deformation is realized by a constant path. Expression (8) represents $\exp_A(\omega t v(A, B))$, the exponential map at A calculated on the vector $\omega t v(A, B)$.

2.2. Rotational Alignment

In some applications, one may wish to only consider alignments under rotations; that is, optimize alignment only over matrices $U \in SO(3)$. The calculations in Section 2.1 can be easily modified, as follows. If $\det\left(V_1 V_2^T\right) > 0$, then $U = V_1 V_2^T \in SO(3)$ and no changes are needed. Otherwise, let the least eigenvalue of Σ occur in the ith diagonal position, $1 \leqslant i \leqslant 3$. Then, change the signs of the entries in the ith column of V_1 to obtain $\tilde{V}_1$ and the sign of the least diagonal entry of Σ to obtain $\tilde{\Sigma}$. The modified matrices allow us to calculate both the geodesic distance and the geodesic interpolation, as in Section 2.1.

2.3. Energy Density

The parametric geodesic path from A to $\hat{B}$ given by (8) has initial velocity $\Lambda'(0) = \omega\, v(A, B)$ and constant speed ω. The energy of the path is given by

$$E(\Lambda) = \int_0^1 \|\Lambda'(t)\|^2\, dt = \|\Lambda'(0)\|^2 = \omega^2 \tag{10}$$

If v_j, $1 \leqslant j \leqslant n$, is the jth column of $v(A, B)$, we have

$$\|\Lambda'(0)\|^2 = \omega^2 \sum_{j=1}^{n} \int_0^1 \left(a\|v_j(s)\|^2 + b\|v_j'(s)\|^2\right) ds\,. \tag{11}$$

Thus, we can interpret the integrand

$$\rho_j(s; A, B) = a\|v_j(s)\|^2 + b\|v_j'(s)\|^2 \tag{12}$$

as the energy density along the jth curve of the arrangement. Observe that ρ_j has been normalized so that $\sum_{j=1}^{n} \int_0^1 \rho_j(s; A, B)\, ds = 1$. Although the shape distance is a measurement that depends on the entire arrangements A and B, the density functions ρ_j, $1 \leqslant j \leqslant n$, describe the local contributions to the total energy and allow us to determine how different parts of the curves in the arrangement contribute to the total shape distance. In particular, it will allow us to trace back regions that exhibit the highest anatomical resemblance or dissimilarity. Examples will be given in Section 3.

3. Arrangements of Sulcal Curves

An arrangement of sulcal curves is an example of a sparse representation of the anatomy of a much more complex structure. This type of representation can be useful in quantifying and modeling large-scale variations in shape across individuals. We employ configurations of sulcal curves to analyze global properties of the shapes of the left and right hemispheres of the brain.

High resolution 1.5T, T1-weighted MRI brain scans (0.86mm x 0.86mm x 1.00mm) from 12 subjects (mean age: 26, 6 females, 6 males) were used. A typical MRI processing pipeline performs intensity corrections in the MRI scan, strips the skull, removes the cerebellum, bisects the cerebral hemispheres, and creates a triangulated surface representing the white matter or the gray matter. We used FreeSurfer [3], a freeware software package available to the neuroscience community to construct topologically correct GM surfaces of each hemisphere for the 12 subjects. Surfaces produced using FreeSurfer have been used to report results from a number of sensory and cognitive tasks, as well as for comparing diseased and control populations. [11, 12, 13, 19].

Gyral ridges and sulcal fundus beds of the cortex anatomically characterize the surface of the brain. A gyrus

is characterized by an area of high positive curvature and a sulcus is characterized by an area of low negative curvature. We computed the curvature at each vertex of S using methods described in [5]. Sulcal paths were then calculated using Dijkstra's algorithm and the cost function

$$c_{ij}^{sulc} = |e_{ij}| \left[\frac{(\kappa_i + \kappa_{max})^2}{2} + \frac{(\kappa_j + \kappa_{max})^2}{2} \right] + |e_{ij}| \frac{(\kappa_i - \kappa_j)^2}{6}, \quad (13)$$

where κ_i and κ_j are the maximal of the principal curvature for the vertices v_i and $v_j \in V$, and $e_{ij} \in E$ is the edge that connects v_i to v_j. Also, κ_{max} is the maximum of the absolute value of the principal curvature for the surface S. This cost function will be minimal when traveling along a sulcal crest line and will penalize traveling along a gyral crestline.

Eight sulci (4 from the right hemisphere and 4 from the left hemisphere) were modeled for each of the 12 gray matter surfaces. The four sulci that were traced on each hemisphere were the central, calcarine, superior frontal and superior temporal. A user identified a start and end point of a sulcus and the fundus of the sulcus was automatically tracked using the principal curvature between these two points. The start and end points of each sulcus were verified by an independent user to reduce variability.

We first illustrate the geodesic interpolation technique. Figure 1 shows two examples of geodesics between the full 8-curve configuration associated with different subjects. In each row, the first and last frames are configurations extracted from MR data and the intermediate frames show several stages of the geodesic interpolation. Corresponding sulcal curves were registered with a fully symmetric variant of the elastic registration techniques of [21, 18], which are based on alignment of velocity fields and implemented via dynamic programming. Starting with a constant-speed parametrization of both curves, one of them was reparameterized using an orientation-preserving diffeomorphism $\gamma\colon I \to I$ that minimizes a cost function, which measures how well the diffeomorphism aligns their tangent fields and penalizes excessive stretching or compression of the curve. This technique leads to undersampling and oversampling of regions of the curve that was reparameterized. To correct for this and obtain more balanced parametrizations of both curves, they were further reparameterized using the arc-length of the graph of γ as a reference. This gives representations of both collections of sulcal curves as arrangements of parametric curves to which we can apply the techniques of Section 2. The metric parameters were set to $a = b = 1$.

We used our shape metrics in experiments in which the goal was to test whether or not it is possible to discriminate the left and right hemispheres of the brain based on anatomical properties captured by arrangements of sulcal curves. The configurations of 8 sulcal curves for the 12 subjects were split up into left and right hemispheres, each containing 4 sulcal curves. Thus, the data consisted of a total of 24 arrangements of curves. We employed two different sets of values for the parameters a and b that define the geodesic metric, namely: (i) $a = 1$ and $b = 0$, which has the effect of not taking the velocity field of the curves into account; (ii) $a = b = 1$, which gives equal weight to position and velocity. For each choice of a, b, we also calculated shape distances allowing general orthogonal alignment and only allowing rotations. Note that, turning off reflections, it should be much easier to distinguish the left and right hemispheres since we expect shape similarity between left and right hemispheres to be much more pronounced if we allow a reflection about the sagittal plane. Due to the limited amount of data, for each arrangement of 4 sulcal curves, we calculated the geodesic distance to all other 23 arrangements and classified the arrangement as representing the left or right hemispheres using the k-nearest-neighbor classifier, for $k = 1, 3, 5$. The results of the experiments are shown in Table 1.

a	b	k	**Reflections**	**Correct Classification**
1	0	1	off	100 %
1	0	3	off	100 %
1	0	5	off	100 %
1	0	1	on	63 %
1	0	3	on	63 %
1	0	5	on	71 %
1	1	1	off	79 %
1	1	3	off	75 %
1	1	5	off	92 %
1	1	1	on	71 %
1	1	3	on	83 %
1	1	5	on	75 %

Table 1. Classification of arrangements of sulcal curves as representing the left or right hemispheres. The parameters a and b determine the metric. Decisions were based on the k-nearest-neighbor classifier.

As expected, the classification performance is much higher if reflections are not allowed during alignment. In this case, the zeroth order metric ($b = 0$) discriminates the two classes very accurately. However, the results seem to also indicate that, even if we allow reflections, configurations associated with the left and right hemispheres can still be distinguished, so that significant shape characteristics intrinsic to the left and right hemispheres exist. In this case, the first-order term in the metric ($b \neq 0$) seems to have an important role. In particular, the experiments suggest that the shapes do not tend to be fully symmetric with respect to the sagittal plane, which may indicate morphological differ-

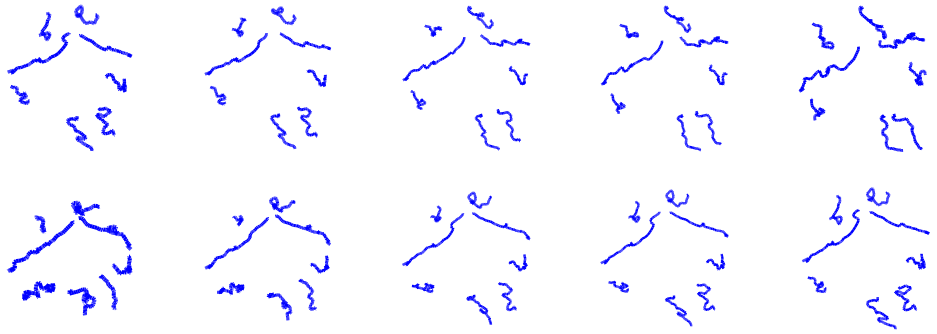

Figure 1. Two examples of geodesic interpolations between sets of eight sulcal curves. In each row, the leftmost and the rightmost configurations were extracted from MR images and the intermediate frames show different stages of the interpolation.

ences associated with function. We illustrate the use of the energy density functions introduced in Section 2.3 to identify the regions that contribute the most to shape differences between the left and right hemispheres of two subjects. We calculated the shape geodesics between the left and right configurations of 4 sulcal curves of two subjects. For each curve, we divided the interval I in ten equal bins and calculated the average value of the energy density in each bin, as shown in Figure 2. The plots are labeled as follows: (a) calcarine; (b) central; (c) superior frontal; (d) superior temporal. The plots indicate that, in both cases, a significant

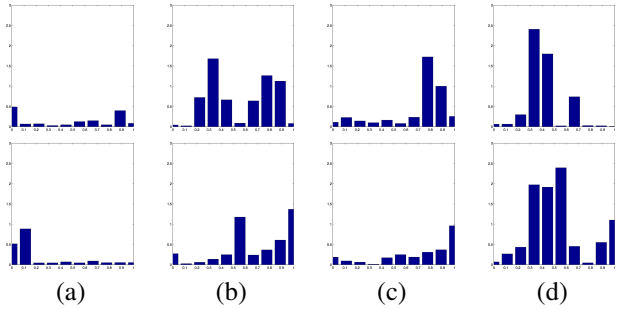

Figure 2. Energy density functions for the following sulci: (a) calcarine; (b) central; (c) superior frontal; (d) superior temporal.

contribution to the total shape distance can be attributed to the middle section of the superior temporal sulcus. To a lesser extent, the same occurs at the "tails" of the central and superior frontal sulci. The most pronounced similarities are observed in the shape of the calcarine and superior frontal curves.

4. Spherical Surfaces

Unlike a curve that has a natural arc-length parametrization, no such special parametrization exists for a spherical surface in 3D space. As a consequence, meshes representing such surfaces tend to exhibit many regions that are either undersampled or oversampled and contain many triangles with undesirable aspect ratios. This is often the case for surfaces whose geometry exhibit intricate features such as those encountered in brain anatomy. To address these issues, parametrizations of spherical surfaces by mappings that minimize the average geometric distortion have been investigated in [15, 10].

4.1. Parametrizations

Let $\mathbb{S}^2$ denote the unit sphere centered at the origin in $\mathbb{R}^3$ and let $\phi\colon \mathbb{S}^2 \to M \subset \mathbb{R}^3$ be a parametrization of a surface M. In [15], the infinitesimal distortion at $x \in \mathbb{S}^2$ due to the mapping ϕ was quantified by the sum of the squares of the singular values of the derivative $d\phi(x)$, the linearization of ϕ at x. However, this measure of distortion is heavily biased towards the larger singular value; that is, it emphasizes stretching and only mildly penalizes compression. This has the practical effect of controlling undersampling of the parametrizations, but not oversampling. An *ad hoc* solution to this problem was proposed in [15], but the cost function utilized is highly asymmetric with respect to stretching and compression. In this paper, we adopt a fully symmetric variant, investigated in [10], that quantifies the local distortion at $p = \phi(x) \in M$, by the quantity

$$\delta(p) = \log^2 \gamma(x) + \log^2 \Gamma(x), \tag{14}$$

where $\gamma(x)$ and $\Gamma(x)$ are the singular values of $d\phi(x)$. The total distortion of ϕ is the average value of δ over M. The details of the construction of minimal distortion parametrizations are similar to those described in [15, 10] and uses a coarse-to-fine approach using the mesh decimation procedure of [7, 17].

Given a triangulated spherical surface M, we remesh it to obtain a more regular triangulation of M, as follows. We first construct a minimal-distortion parametrization ϕ of M. Then, we take a "regular" mesh of the sphere and transfer the triangulation of $\mathbb{S}^2$ to M, which leads to a better mesh of M. This construction also allows us to parameterize different spherical surfaces over a fixed spherical mesh

of $\mathbb{S}^2$, which gives a common domain for shape comparison. Figure 3(a) shows a triangular mesh representing the surface of a cerebellum extracted from an MR image with 28,340 vertices. The mesh obtained via a minimal distortion parametrization is shown in Figure 3(b) and has much more regular triangles. Close-up views are shown in panels (c) and (d). A similar example for the gray matter surface of the entire left hemisphere of a brain is shown in Figure 4. The original mesh has 191,724 vertices and was remeshed at two different resolutions: 163,842 and 40,962 vertices, respectively.

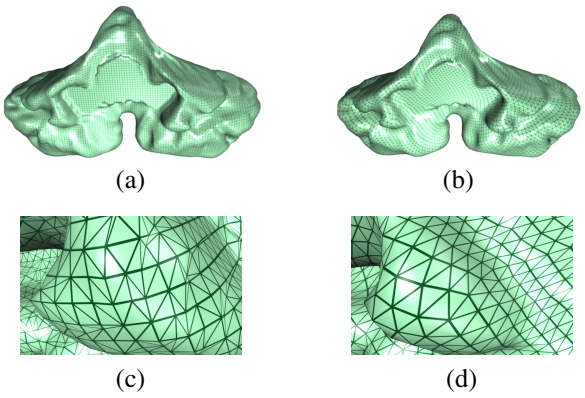

Figure 3. Remeshing the surface of a cerebellum: (a) the original mesh with 28,340 vertices; (b) remeshing with a minimal distortion parametrization; (c) close-up view of the original mesh; (d) close-up view of the remeshed surface.

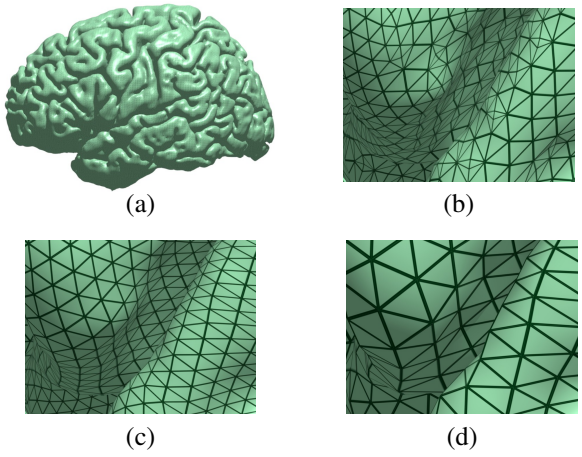

Figure 4. Remeshing the GM surface of the left hemisphere of a brain: (a) the original mesh with 191,724 vertices; (b) close-up view of the original mesh; (c) close-up view of the remeshed surface with 163,842 vertices; (d) close-up view of the surface remeshed at a lower resolution with 40,962 vertices.

Once a global parametrization $\phi\colon \mathbb{S}^2 \to M$ is available, we can easily decompose the surface M into spatial curves at any desired resolution. For example, if we decompose $\mathbb{S}^2$ into a family of disjoint parallels, we can transfer the decomposition to M via the mapping ϕ, as illustrated with a cerebellum on the first row of Figure 5. A similar decomposition of the left hemisphere of a brain is shown on the second row.

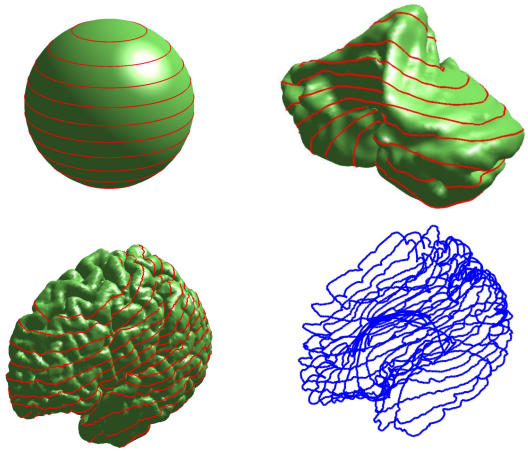

Figure 5. Decomposition into space curves.

4.2. Shape Alignment

In order to compare the shapes of two surfaces presented by minimal-distortion parametrizations $\phi^i\colon \mathbb{S}^2 \to M_i$, $i = 1, 2$, we first need to align their geometric features. As in [10], we consider alignments obtained via reparametrizations by rotations. Given a rotation matrix $R \in SO(3)$, we consider reparametrizations of a parametric $\phi\colon \mathbb{S}^2 \to M$ of the form

$$p \mapsto \phi(R^T p), \tag{15}$$

which simply rotates the sphere $\mathbb{S}^2$ before mapping it to M via ϕ. We denote this new parametrization of M by ϕ_R. Note that the singular values of $J_\phi^{-1}(x)$ and $J_{\phi_R^{-1}}(x)$ are the same, for any $x \in M$. Thus, if ϕ is a minimal-distortion parametrization, so is ϕ_R.

The surface alignment criterion adopted is based on the average discrepancy of the outer normal unit fields. For a rotation matrix R, think of $\phi^1(x) \in M_1$ and $\phi_R^2(x) \in M_2$ as corresponding points. We wish to measure the average discrepancy of the normal fields $N_1(p)$ and $N_2(p; R)$, for $p \in \mathbb{S}^2$. Normal fields are insensitive to translations and scale, but they do change under rotations and reflections of a surface. Thus, before comparing the normal fields of ϕ_1 and ϕ_R^2, we find the orthogonal matrix $U_R \in O(3)$ that minimizes

$$\iint_{\mathbb{S}^2} \|N_1(p) - U_R\,(N_2(p; R))\|^2\, dS(p). \tag{16}$$

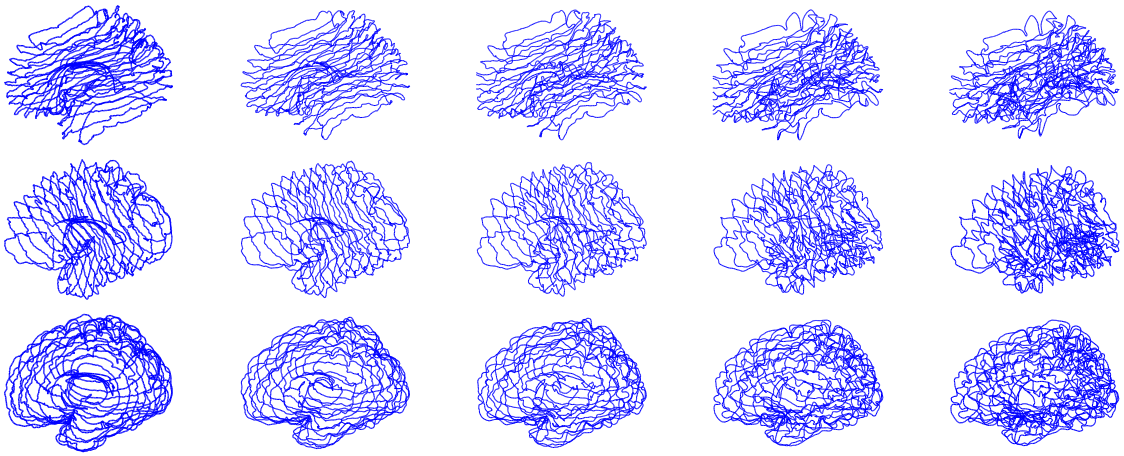

Figure 6. Each row shows a geodesic between arrangements of curves representing the left hemispheres of two aligned brains. Three different decompositions into space curves of the same pair of brains have been used.

This problem is similar to rotational alignment in Procrustes shape analysis and the solution can be obtained in closed form [9]. Thus, the alignment problem is reduced to finding $R \in SO(3)$ that minimizes (16). To solve this minimization problem, we first sample $SO(3)$ "uniformly" over a large set of rotations and evaluate the cost function. Subsequently, a local refinement near the top candidates is conducted using a gradient search. The local search in $SO(3)$ can be implemented efficiently using its Lie group structure.

4.3. Experiments

We applied the parametrization and alignment techniques to the surfaces of the left hemisphere of the brains of two subjects S_1 and S_2. The original meshes had 146,992 vertices for S_1 and 191,724 vertices for S_2. Minimal-distortion parametrizations were constructed for both surfaces, which were then remeshed with 40,962 vertices. The parametric surfaces were aligned so that the decompositions of the surfaces into curves using parallels of $\mathbb{S}^2$ yield arrangements of curves that can be used for shape comparison. The surfaces were decomposed compatibly into space curves using three different sets of parallels (corresponding to different choices of north and south poles) and the geodesic interpolations between the corresponding arrangements were calculated using the techniques of Section 2. The three geodesics (calculated with parameter values $a = b = 1$) are shown in Figure 6.

5. Discussion

We employed arrangements of space curves to represent the anatomy of the brain and its substructures at various different resolutions. A shape theory of arrangements of curves was developed as well as computational tools to calculate shape distances and geodesics. Used in conjunction with curve and surface alignment methods, the metric allows us to quantify morphological similarity and difference. Techniques were also devised to identify particular regions where shape similarity and divergence are most pronounced. The algorithms were applied to the analysis of the shape of configurations of sulcal curves and to the geodesic interpolation of cortical surfaces. Registration techniques were also used to decompose spherical surfaces into space curves in a compatible manner.

The human cortex is a highly complex structure, both in terms of its functions and its shape. Detecting or identifying anatomical variations can ultimately aid our understanding of how the brain may change with aging or with disease. In this study, we have successfully been able to use the geometry of sulcal curves to discriminate between left and right cortical hemispheres and identify areas where some of the main anatomical differences occur. Being able to detect, quantify and model left-right differences in cortical shape has implications for tracking changes in the cortex that may occur with functional deficits (such as language or hearing impairment) or in disease. Another application of these results is the verification or confirmation of which hemisphere of the cortex is the left and right hemisphere. Although this may seem a trivial application, there currently is no standard as to whether MRI data is stored in radiological format or neurological format. As data becomes publicly available through databases, inevitably errors will occur as to how data is stored and represented. The results presented here can serve as an approach to verifying the reliablity of the data. However, the real promise of these preliminary results lies in understanding the shape of the cortex, which has implications for the study of healthy and diseased populations. The shape metrics and interpolation techniques developed will be useful in defining and calculating mean

shapes, variance and other shape statistics, in the development of full statistical models of normal shape variations observed across multiple subjects, as well as shape variations due to disease. These topics will be investigated in future work.

Acknowledgments

This work was supported in part by NSF grants CCF-0514743 and DMS-0101329, and NIH grant P20 EB02013. We thank D. Rottenberg (Departments of Radiology and Neurology, University of Minnesota) for providing the MRI data and A. Kline for processing some of the MRI data.

References

[1] G. Bartzokis, J. L. Cummings, D. Sultzer, V. W. Henderson, K. H. Nuechterlein, and J. Mintz. White matter structural integrity in healthy aging adults and patients with alzheimer disease: A magnetic resonance imaging study. *Arch. Neurol*, 60:393–398, 2003.

[2] J. G. Csernansky, M. K. Schlindler, N. R. Splinter, L. Wang, M. Gado, L. D. Selemon, D. Rastogi-Cruz, J. A. Psener, P. A. Thompson, and M. I. Miller. Abnormalities of thalamic volume and shape in schizophrenia. *Am. J. Psychiatry*, 161:896–902, 2004.

[3] A. M. Dale, B. Fischl, and M. I. Sereno. Cortical surface-based analysis I: Segmentation and surface reconstruction. *Neuroimage*, 9:179–194, 1999.

[4] H. A. Drury, D. C. Van Essen, M. Corbetta, and A. Z. Snyder. Surface-based analyses of the human cerebral cortex. In A. Toga et al., editors, *Brain Warping*, pages 337–363. Academic Press, 1999.

[5] B. Hamann. Curvature approximation for triangulated surfaces. In G. Farin, H. Hagen, and H. Noltemeier, editors, *Geometric Modelling in Computing Supplementum 8*, pages 139–153. Springer-Verlag, New York, 1993.

[6] N. A. Honeycutt, A. Musick, P. E. Barta, and G. D. Pearlson. Measurement of the planum temporale (PT) on magnetic resonance imaging scans. *Psychiatry Res.*, 98:103–116, 2000.

[7] K. Hormann, G. Greiner, and S. Campagna. Hierarchical parametrization of triangulated surfaces. In *Vision, Modeling, and Visualization*, pages 219–226, 1999.

[8] L. Jancke, J. Hanggi, and H. Steinmetz. Morphological brain differences between adult stutterers and non-stutterers. *BMC Neurology*, 4:23, 2004.

[9] D. G. Kendall. Shape manifolds, Procrustean metrics and complex projective spaces. *Bulletin of London Mathematical Society*, 16:81–121, 1984.

[10] X. Liu, J. C. Bowers, and W. Mio. Parametrization, alignment and shape of spherical surfaces. In *Second International Conference on Computer Vision Theory and Applications*, volume 1, pages 199–206, 2007.

[11] L. F. Lyoo, Y. H. Sung, S. R. Dager, S. D. Friedman, J. Y. Lee, S. J. Kim, N. Kim, D. L. Dunner, and P. F. Renshaw. Regional cerebral cortical thinning in bipolar disorder. *Bipolar Disorders*, 8:65–74, 2006.

[12] M. Martinussen, B. Fischl, H. B. Larsson, J. Skranes, S. Kulseng, T. R. Vangberg, T. Vik, A. M. Brubakk, O. Haraldseth, and A. M. Dale. Cerebral cortex thickness in 15-year-old adolescents with low birth weight measured by an automated MRI-based method. *Brain*, 128:2588–2596, 2005.

[13] M. R. Milad, B. T. Quinn, R. K. Pitman, S. P. Orr, B. Fischl, and S. L. Rauch. Thickness of ventromedial prefrontal cortex in humans is correlated with extinction memory. *Proceedings of the National Academy of Sciences of the United States of America*, 102:10706–10711, 2005.

[14] V. Penhune, R. Zatorre, J. MacDonald, and A. Evans. Interhemispheric anatomical differences in human primary auditory cortex: probabilistic mapping and volume measurement from magnetic resonance scans. *Cerebral Cortex*, 6:661–772, 1996.

[15] E. Praun and H. Hoppe. Spherical parametrization and remeshing. In *ACM SIGGRAPH 2003*, pages 340–349, 2003.

[16] D. H. Salat, R. L. Buckner, A. Z. Snyder, D. N. Greve, R. S. Desikan, E. Busa, J. C. Morris, A. M. Dale, and B. Fischl. Abnormalities of thalamic volume and shape in schizophrenia. *Am. J. Psychiatry*, 161:896–902, 2004.

[17] P. Sander, S. Gortler, S. Snyder, and H. Hoppe. Signal-specialized parametrization. In *Eurographics Workshop on Rendering*, pages 87–100, 2002.

[18] T. B. Sebastian, P. N. Klein, and B. B. Kimia. On aligning curves. *IEEE Transactions on Pattern Analysis and Machine Intelligence*, 25(1):116–125, 2003.

[19] H. Shiraishi, S. P. Ahlfors, S. M. Stufflebeam, K. Takano, M. Okajima, S. Knake, K. Hatanaka, S. Kohsaka, S. Saitoh, A. M. Dale, and E. Halgren. Application of magnetoencephalography in epilepsy patients with widespread spike or slow-wave activity. *Epilepsia*, 46:1264–1272, 2005.

[20] I. Sigalovsky, B. Fischl, and J. Melcher. Mapping an intrinsic MR property of gray matter in auditory cortex of living humans: a possible marker for primary cortex and hemispheric differences. *Neuroimage*, 32:1524–1437, 2006.

[21] H. D. Tagare. Shape-based non-rigid correspondence with applications to heart motion analysis. *IEEE Trans. on Medical Imaging*, 8(7):570–579, 1999.

[22] P. M. Thompson, C. M. Hare, and W. R. Lees. Dynamic mapping of human cortical development during childhood through early adulthood. *Proc. National Academy of Sciences*, 101:8174–8179, 2004.

[23] P. M. Thompson, K. M. Hayashi, G. L. De Zubicaray, A. L. Janke, S. E. Rose, J. Semple, M. S. Hong, D. H. Herman, D. Gravano, D. M. Doddrell, and A. W. Toga. Mapping hippocampal and ventricular change in alzheimer disease. *Neuroimage*, 22:1754–1766, 2004.